Research Paper

Ionospheric behaviors and characteristics in Asian sector during the April 2023 geomagnetic storm with multi-instruments observations

Linlin Li [a,b], Shuanggen Jin [a,c,*]

[a] *Shanghai Astronomical Observatory, Chinese Academy of Sciences, Shanghai, 200030, China*
[b] *School of Astronomy and Space Science, University of Chinese Academy of Sciences, Beijing, 100049, China*
[c] *School of Surveying and Land Information Engineering, Henan Polytechnic University, Jiaozuo, 454003, China*

ABSTRACT

Geomagnetic storms frequently affect satellite navigation, communication and satellite orbits. Monitoring and understanding the ionospheric disturbances and responses to geomagnetic storms are crucial. The detailed ionospheric responses and physical mechanisms to various geomagnetic storms, however, have not yet been extensively studied. In this paper, the ionospheric variation behaviors and features following the April 2023 magnetic storm along the Asian sector are thoroughly studied using multi-instrument observation data, including the Global Navigation Satellite System (GNSS), ionosonde, and other satellites. Large-scale Traveling Ionospheric disturbances (LSTIDs) are observed from BeiDou Geostationary Earth Orbit (GEO) satellites, GPS and GLONASS. LSTIDs traveled with a speed of 760–1300 m/s from high latitude region to low latitude region with a period of about 40 min. The equatorial propagating LSTIDs were generated by coronal mass ejections (CMEs), which occurred in April 2023 with periodic energy input from the auroral area. The poleward LSTIDs are also observed with a velocity of approximately 600–750 m/s and the period is similar. Neutral wind also influenced the characteristics of the ionospheric response. The $[O]/[N_2]$ ratio declined during the storm, which led to the formation of the negative storm phases. The largest vertical total electron content (VTEC) is found, and the strengthened region of TEC is mainly centered between $\pm 20°$ within geographical latitude. Equatorial Ionospheric Anomaly (EIA) is also observed, which is probably influenced by the electric field. As the time goes on, the peak on the south side of the EIA is disappearing. Meanwhile, the height of the ionospheric maximum electron density rises, and the electron density falls.

1. Introduction

A geospace storm is a storm that interacts harmoniously in the magnetic field (magnetic storm), ionosphere (ionospheric storm), atmosphere or thermosphere (atmospheric storm), and electric field of atmospheric-ionospheric-magnetospheric origin according to Chernogor and Rozumenko (2008) and Chernogor (2011) system paradigm. Geomagnetic storms occur when the energy from the solar wind is transported into the space surrounding the Earth, resulting in dynamic interactions. Large geomagnetic storms will cause hazards (Skone and Yousuf, 2007; Astafyeva et al., 2014). Violent ionospheric disturbances may disrupt radio communications and degrade the navigation accuracy (Su et al., 2019). Particularly, low Earth orbit satellites, especially below 500 km, are greatly affected during geomagnetic storms. When a coronal mass ejection (CME) approaches the Earth, the energy is injected into

the Earth's pole region. The energy is then transported to the upper atmosphere, where it heats up and spreads to low-latitude areas. The expansion of the lower atmosphere leads to an increase in atmospheric density around satellite orbits, causing increased resistance and resulting in a decrease in speed and altitude for satellites, which make it challenging to maintain their original positions. Short-wave communication is a kind of communication that is mainly dependent on the ionosphere. When a geomagnetic storm occurs, the distribution of ionospheric electron density varies dramatically, causing a shift in the reflectivity of radio waves of various frequencies, and resulting in the abnormal reflection of radio waves of higher frequencies. If the short-wave propagation signal is utilized without the geomagnetic storm at this time, the signal received by the original receiving point of the radio wave will be considerably weakened or even not received, resulting in the stoppage of short-wave communication. Therefore, it is

crucial to observe and understand ionospheric disturbances during different geomagnetic storms. However, ionospheric reactions to different geomagnetic storms are complex, and the fundamental causes remain unknown clearly. At present, monitoring and understanding ionospheric disturbances during magnetic storms are still hot and important topics in space sciences.ic

For ionospheric study, there are several instruments available to observe and analyze the ionospheric variation characteristics from different dimensions. Ionosonde, sounding rockets, incoherent scatter radar, and other observational techniques have been widely utilized to observe and investigate the ionospheric variations and responses (Nicolls et al., 2004; Ren et al., 2022; Tang et al., 2022). However, establishing a dense ionospheric monitoring network is still challenging due to high costs and hard-reaching areas. In recent years, dual- or multi-frequency Global Navigation Satellite System (GNSS) has emerged as a valuable tool for measuring ionospheric TEC and its disturbances (Jin et al., 2006; Jin and Park, 2007), particularly during magnetic storms. Dense multi-GNSS observation networks can cover and monitor the entire ionosphere when compared to other traditional observation techniques. GNSS observations provide high spatial and temporal resolution ionospheric TEC data, which are important for ionospheric delay correction and space environment monitoring (Heise et al., 2002). With GNSS observation data, a number of studies on ionospheric variations were conducted in different aspects such as earthquake, geomagnetic storms, volcano, Typhoon, etc (Heki and Enomoto, 2015; Liu et al., 2019; Shinbori et al., 2022; Jin et al., 2022). Geodesy, space physics, and other fields have paid particular attention to the study and monitoring of ionospheric variations with GNSS (Alizadeh et al., 2011).

Traveling ionospheric disturbance (TID) is one of the important ionospheric anomalies, which are usually divided into two types based on propagation characteristics such as velocity and period. The first type is the large-scale traveling ionospheric disturbances (LSTIDs) with a horizontal wavelength of more than 1000 km, a propagation speed of 400–1000 m/s, and the propagation duration of roughly 30–180 min (Hunsucker 1982; Tsugawa et al., 2003). The second one is middle-scale traveling ionospheric disturbances (MSTIDs), which are more commonly observed. The horizontal wavelength of the MSTIDs is several hundred kilometers, the propagation speed is 100–250 m/s, and the propagation time is 15–60 min. Previous studies have shown that TIDs were results from various sources, including meteorological activity and space weather events. Geomagnetic storms, for example, can significantly increase energy and momentum in the auroral zone through joule heating, precipitation particles, and the Lorentz force. These energy deposits can produce large-amplitude atmospheric gravity waves (AGWs), which manifests as LSTIDs in the ionosphere (Hines, 1960; Hocke and Schlegel, 1996). The LSTIDs excited by the auroral region can move to the equator and interact with the background ionosphere while undergoing various changes. For example, the energy dissipation may be caused by the ion drag (Tsugawa and Saito, 2004) and the influence of the neutral wind, which can change the propagation speed and period (Ding et al., 2007). During a geomagnetic storm, TIDs from the polar region can perturb the middle and low latitude ionosphere. Tsugawa et al. (2003) found that the damping rates of TIDs were predominantly influenced by the ion-neutral collision frequency associating with the ion drag. Horvath and Lovell (2009) demonstrated how energy from the auroral region can heat the thermosphere and induce equatorward winds, resulting in powerful LSTIDs. As for MSTIDs, the sources include the energy injected into the polar region, changes in tropospheric systems (Valladares and Hei, 2012), and the solar terminator (Somsikov, 1987).

Extensive GNSS receiver networks have been utilized to investigate LSTIDs features in Japan, North America, and Europe, with numerous reports on the response to geomagnetic storms. Nowadays, the BDS satellite observation data are accessible, and BDS GEO satellites can continuously monitor ionospheric variations at line-of-sight. Furthermore, no two storms are alike (Emelyanov et al., 2023) and the

ionospheric variation also exhibits complex disturbance characteristics as a result of different events. The velocity, amplitude, period and the direction of the TIDs are the critical and different cases studies can help us better understand the physical mechanism behind. Although there are many studies on the first three aspects, most TIDs spread from high latitude to low latitude. However, poleward TIDs are not always mentioned in the previous study, and it is essential to pay attention to the poleward TID features and to better understand the electrodynamics during the magnetic storm. Thus, more instruments and dense networks are required to study and understand ionospheric disturbance features during the geomagnetic storms.

Currently it is a new solar activity peak, which has the potential to impact the ionosphere significantly. On 23–24 April 2023, a super geomagnetic storm was occurred, which is the largest one since December 2019. The observed data from more types of equipments might be complementary to one alone and allow us to investigate geomagnetic storm features in greater details. Particularly, BDS GEO satellites provide a good opportunity to continuously monitor ionospheric variations at line-of-sight, such as detailed east-west ionospheric disturbances. Furthermore, most case studies were concentrated on the equatorward TID, while the existing poleward TID is not clear. In this paper, the ionospheric variation behaviors and features following the April 2023 geomagnetic storm along the Asian sector are thoroughly investigated using multi-instrument data, including GNSS, ionosonde, and other satellites in details. In particular, LSTIDs are studied from BeiDou Geostationary Earth Orbit (GEO) satellites, GPS and GLONASS observation data. Section 2 introduces data and methods. Results and analysis are presented in Section 3. The discussion is provided in Section 4, and finally conclusions are summarized in Section 5.

2. Data and methods

2.1. Observation data

The solar activity is entering its 25th activity period since December 2019. There are more solar activities that cause many complex changes to the space environment. Fig. 1 shows the space weather and geophysical conditions from 21 to 27 April 2023, which covers the main phase and recovery phase of this geomagnetic storm. The main phase is between the blue line and the red line, and the recovery phase is shown after the red line. The minimum of Dst is about −212 nT on April 24, 2023 at 05:30 and the maximum of Kp is 8 on that day, which means that this event is a G4 super magnetic storm. The $F_{10.7}$ is between 130 and 155 in numerical terms. The SSN on April 22, 2023 is 98 and becomes 80 on April 23, 2023. From 24 to 25 April it is 72, and then rises to 96 on 26 April. Ap index is from 2 to 67. Between 17:44–18:44 on April 22, 2023, an M1.7 solar flare erupted and caused CME, which is the direct source of the 23–24 April 2023 super geomagnetic storm.

In this study, the data are used from GNSS observations, Global Ionospheric Map (GIM), ionosonde, and other satellite observation data. The details are shown as follows.

1) GNSS observation data along Asian sector are used for calculating TEC and its variations in the term of the velocity, direction, and period. Here the BeiDou Navigation Satellite System (BDS) GEO satellite observation data is from International GNSS Service (IGS) Multi-GNSS experiment (MGEX) stations (https://cddis.nasa.gov/archive/gnss/data/daily/). GPS and GLONASS data are collected from Crustal Movement Observation Network of China (CMONOC). BDS GEO data allow us to estimate the light-of-sight shift in the ionosphere, which better know and understand the propagation and characteristics of the ionospheric disturbances during the geomagnetic storm.
2) Global Ionospheric Map (GIM) data was downloaded from IGS products (https://cddis.nasa.gov/archive/gnss/products/ionex/),
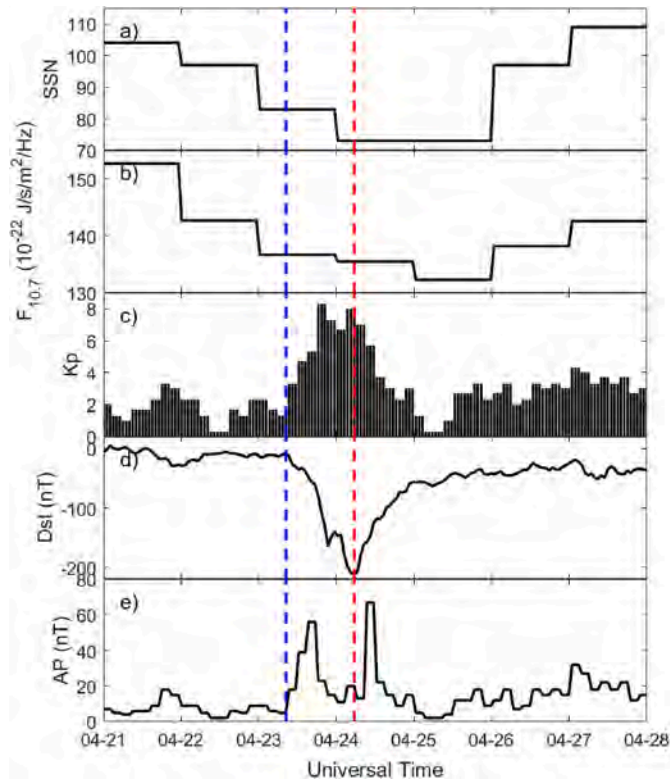
Fig. 1. Space weather and geophysical conditions from 21 to 27 April 2023 for the sunspot number (a), $F_{10.7}$ (b), Kp (c), Dst (d), and Ap (e), respectively. The main phase is between the blue line and the red line. The recovery phase is after the red line. (For interpretation of the references to colour in this figure legend, the reader is referred to the Web version of this article.)

which provide global TEC distribution with $2.5° \times 5°$ and 1 h interval.

3) $[O]/[N_2]$ data are obtained from the Global Ultraviolet Imager (GUVI) on board the Thermosphere, Ionosphere, Mesosphere Energetics and Dynamics (TIMED) satellite, which provided information on the composition of the thermospheric $[O]/[N_2]$ composition (https://imag-data.bgs.ac.uk/GIN_V1/GINForms2). According to Christensen et al. (2003), TIMED has an orbit height of approximately 625 km and an inclination of 74°. $[O]/[N_2]$ can be used to characterize changes in thermosphere composition driven by geomagnetic changes (Cai et al., 2021; Crowley et al., 2006)

4) Electron density data are from Swarm and Constellation Observing System for Meteorology, Ionosphere and Climate (COSMIC). The Swarm mission consists of three identical satellites named Alpha, Bravo, and Charlie (A, B and C). Swarm A and C make up the lowest pair of satellites, which are positioned at an altitude of 462 km and an inclination angle of 87.35°, and are separated by 1.4° in longitude at the equator initially. Swarm B is flying at a higher orbit of 511 km and 87.75° inclination angle initially. In this study, the electron density data is from Langmuir probe data, which can provide electron temperature and plasma density at the same time. The Swarm data are available from https://vires.services/#Data. The COSMIC consists of six microsatellites with around 100 min to circle the Earth. The COSMIC data are downloaded from COSMIC Data Analysis and Archive Center (CDAAC, https://cdaac-www.cosmic.ucar.edu/cdaac/index.html).

5) F2 layer critical frequency (foF2) data in Asian sector are attained from 4 ionosonde stations in China, namely Mohe, Wuhan, Beijing and Hongkong. The time resolution is 15 min and the data are available in the Data Centre for Meridian Space Weather Monitoring Project.

6) Space weather parameters like sunspot number, $F_{10.7}$, Kp, Dst, Ap, and other ACE data are available on Coordinated Data Analysis Web (CDAWeb) (https://cdaweb.gsfc.nasa.gov/index.html/).

2.2. Methods

Fig. 2 illustrates the ground-based multi-instruments locations employed in the analysis of the ionospheric disturbance characteristics following the geomagnetic storm. The black dots represent GNSS stations that provide GPS and GLONASS observation data and the blue dots correspond to the MGEX stations that provide observation data of BDS GEO satellites. Additionally, two BDS GEO satellites (C01 and C03) are marked with orange and gray point in the map. Ionosondes in Heilongjiang Mohe, Beijing Changping, Wuhan Zuolingzhen, and Hainan Fuke are represented by green squares.

With dual-frequency GNSS observations, slant TEC (STEC) can be obtained with Eqs (1) and (2) below (Brunini and Azpilicueta, 2009; Jin et al., 2017).

$$STEC = \frac{f_1^2 f_2^2}{40.3(f_1^2 - f_2^2)}(L_1 - L_2 + \lambda_1(N_1 + b_1) - \lambda_2(N_2 + b_2) + \varepsilon_L) \quad (1)$$

$$STEC = \frac{f_1^2 f_2^2}{40.3(f_1^2 - f_2^2)}(P_1 - P_2 - (d_1 - d_2) + \varepsilon_P) \quad (2)$$

where STEC is the slant total electron content with unit TECU (1 TECU $= 10^{16}$ el/m^{-2}), L_1 and L_2 are the GPS carrier phase measurements in frequency f_1 and f_2, P_1 and P_2 are the GPS code measurements in frequency f_1 and f_2, N is the ambiguity, b is the instrument biases for carrier phase, d_1 and d_2 are the differential code bias, and ε is the residual.

The VTEC can be obtained from the STEC through Mapping Function (MF) by Eq (3).

$$MF(E) = \frac{STEC}{VTEC} = \frac{1}{\cos \alpha} = \frac{1}{\sqrt{1 - \left(\frac{R_{earth}}{R_{earth} + H_{ion}} \cos(E)\right)^2}} \quad (3)$$

where R_{earth} is the Earth radius, H_{ion} is the height of single shell iono-
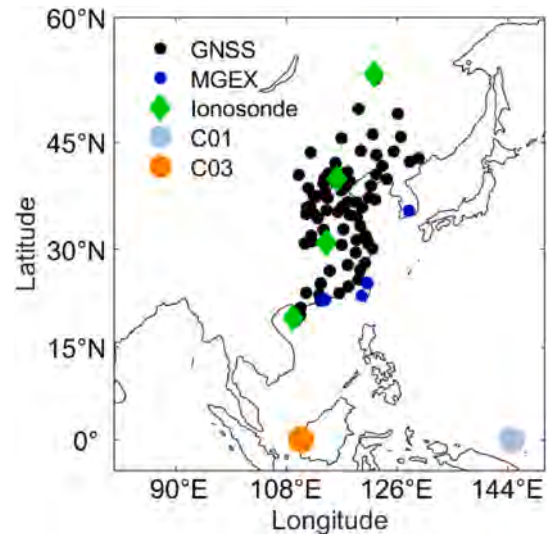
Fig. 2. The location of multi-instrument stations and GNSS stations. GNSS stations that offer GPS and GLONASS observation data are represented by black dots. MGEX stations, shown as the blue dots, provide BDS observation data. The ionosondes are marked as green diamonds. The gray and orange dots are BDS GEO satellites C01 and C03, respectively. (For interpretation of the references to colour in this figure legend, the reader is referred to the Web version of this article.)

sphere, which is set as 350 km in this study, α is the zenith distance of the satellite relative to the ionosphere piercing point (IPP), and E is the altitude angle of the satellite relative to the receiver.

Finally, the fourth-order Butterworth filter is employed to obtain the filtered VTEC and the ionospheric disturbance is precisely estimated.

3. Results and analysis

3.1. TEC variations from GIM

Fig. 3 shows the behavior of ionospheric TEC variations obtained from GIM and its deviation over the Asian sector (along 120E, geographic longitude) during 22–26 April 2023. It can be found that on 24 April, the maximum VTEC enhancement occurred, and the enhanced area of TEC is mainly localized between $\pm20°$. The peaks on both sides were strengthened during UT = 0–6 on 24 April, which was the EIA. The peak on the south side of the EIA was disappeared as the time went by. But the northern peak still exists between 6 and 12 UT at approximately 20°N. It was found that positive and negative ionospheric storms were occurred during the main and recovery phases. In the main phase, TEC had a significantly increase in the middle and low latitudes. Meanwhile, between UT = 3–10, the TEC in the southern hemisphere's mid-latitude was decreased, whereas the TEC in the mid and low latitudes between UT = 7–18 was decreased. The TEC at high latitudes in the northern and southern hemispheres was also reduced, while the range of TEC reduction was larger in the northern hemisphere.

3.2. TIDs characteristic from multi-GNSS

Three GEO satellites (C01, C02 and C03) are selected because most of the pairs' elevation angles are between 30 and 60°, which is more suitable for ionospheric studies. The positions of the satellites are shown in Fig. 2. Figs. 4–5 show the filtered TEC and the elevation angles of

different pairs of BDS GEO satellites and stations. The left of each figure is the filtered TEC in TECU, while the elevation angle in degrees is marked on the right.

With BDS observation data, TIDs are detected during the main phase and the recovery phase and apparent disturbances are appeared during UT = 20–24 on 23 April and UT = 3–8 on 24 April. Additionally, the amplitude of the disturbance near the minimum Dst (at the time at the end of the main phase) is larger than other time during 23–24 April 2023. Meanwhile, it is also found that the main period of TIDs during the main phase is about 40 min. GPS and GLONASS observation data are used to improve the amount of data and reduce inaccuracy in estimating TID propagation velocity in the north-south direction.

For pairs of GEO satellites and ground stations, the ionospheric pierced pints (IPPs) could be approximated as unchanging, and the location of IPPs are reported in Table 1. The IPPs longitude is variable for different GEO satellites and the same station, but the latitude is similar. Fig. 6 presents the filtered VTEC from different stations paired with C01 and C02 at 28.4°N. Despite the fact that WUH2, WUHN, and JFNG are all at the same latitude, the amplitude for C01 is greater than C03. The elevations of these stations and C01 pairs are within 40–50°, and they are about 50–60° for C03 pairs. This reconfirmed that different pairs of stations have varying amplitudes, which could be connected to the geometry. Besides, it is also found that the TIDs reach 28.4°N at the same time during 114°–117.3°E. Thus, the geomagnetic field does not affect the TID propagation strongly in this region.

According to GPS and GLONASS, the travel gram in Fig. 7 indicates that the velocity is roughly 866 m/s – 1000 m/s with G29 from UT = 20 h to UT = 24 h. Also, the velocity ranges from approximately 924 m/s to 1100 m/s for G01, G21, and R14 from UT = 0–8 h. The propagation direction of these TIDs is primarily from high latitude to low latitude. TIDs propagating equatorially was originated in the auroral region. Fig. 8 shows two kinds of velocity on April 24, 2023 from G14. The first one emerges between 28 and 45N and the velocity is about 760m/s-

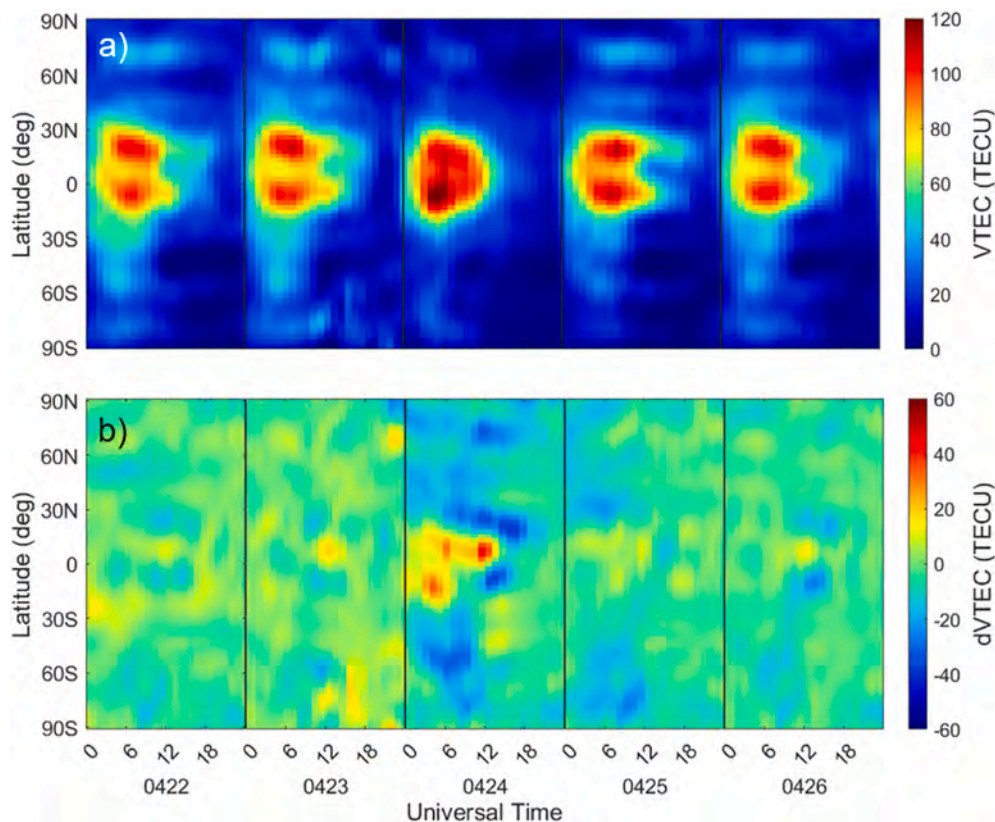**Fig. 3.** (a) VTEC and (b) the deviation of VTEC from 22 to 26 April 2023 over Asian longitude sector along 120°E.
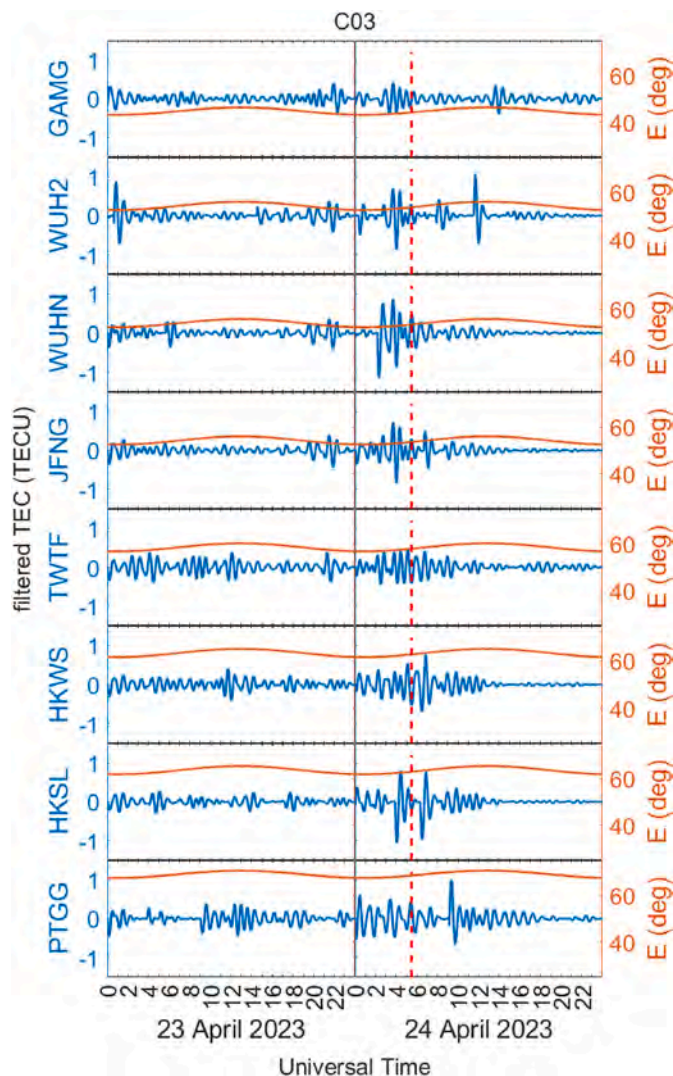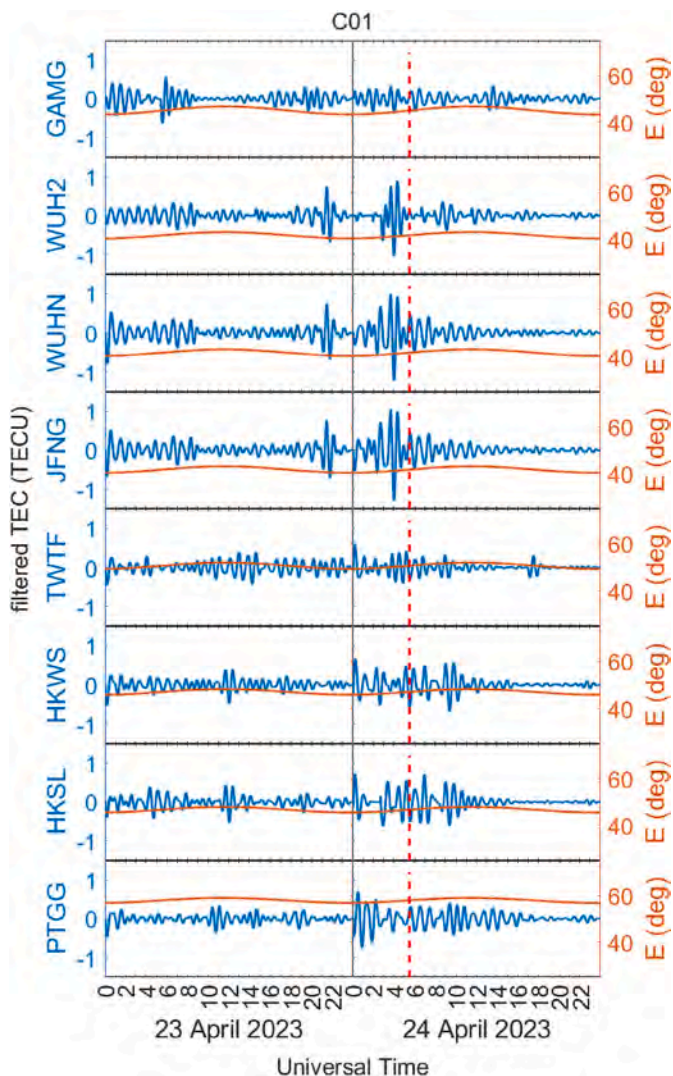
Fig. 4. VTEC from different stations with C01 are blue lines and the orange lines are elevation angles from 23 to 24 April 2023. The red line represents the minimum moment of Dst index. (For interpretation of the references to colour in this figure legend, the reader is referred to the Web version of this article.)

Fig. 5. VTEC from different stations with C03 are blue lines and the orange lines are elevation angles from 23 to 24 April 2023. The red line represents the minimum moment of Dst index. (For interpretation of the references to colour in this figure legend, the reader is referred to the Web version of this article.)

1300 m/s, which is also the equatorward TID. The other is poleward TIDs, which has a velocity of roughly 600–750 m/s and appears between 20 and 28N. The poleward propagating TIDs might come from geomagnetic equator region. As indicated in prior works, Habarulema et al. (2015 and 2016) thought that the poleward TIDs were due to ionospheric electrodynamics, especially changes in $\vec{E} \times \vec{B}$ vertical drift after the storm. The LSTID propagation periods are about 40 min.

As it is well-known, the TIDs are the result of the AGWs propagating in the ionosphere. In addition, photochemistry and electrodynamics have an impact on the ionospheric variation characteristics. Thus, the photochemistry could be the reason for the variation between the higher and lower latitudes particularly.

3.3. Electron density variations

Four ionosonde stations observation data in China are obtainable, including Heilongjiang Mohe, Beijing Changping, Wuhan Zuolingzhen, and Hainan Fuke. Fig. 9 shows the f_oF_2 from the stations. According to the space weather indexes in Fig. 1, the April 21, 2023 is the quiet day, which is chosen as the reference day. The relationship of f_oF_2 and N_mF_2 is shown below (Ma et al., 2012):

Table 1
The location of station and GEO satellite ionospheric pierced points.

Station\ PRN	Latitude (°)		Longitude (°)	
	C01	C03	C01	C03
GAMG	33.0	33.0	129.5	126.3
WUH2	28.4	28.4	117.1	114.0
WUHN	28.4	28.4	117.1	114.0
JFNG	28.3	28.4	117.3	114.2
TWTF	23.3	23.3	123.0	120.4
HKWS	20.9	21.0	116.8	114.1
HKSL	20.9	20.9	116.4	113.7
PTGG	13.6	13.6	122.7	120.3

$$N_mF_2 = \frac{1}{80.6}(f_oF_2)^2 \qquad (4)$$

where the unit of N_mF_2 is m^{-3} and that of f_oF_2 is Hz. The N_mF_2 is proportional to $f_oF_2^2$. As a result, it can be seen that the Asian sector experienced a strong negative storm response because the crucial frequency fell dramatically below the background average level, and higher latitude ionospheric disturbances are more severe. The foF2 was
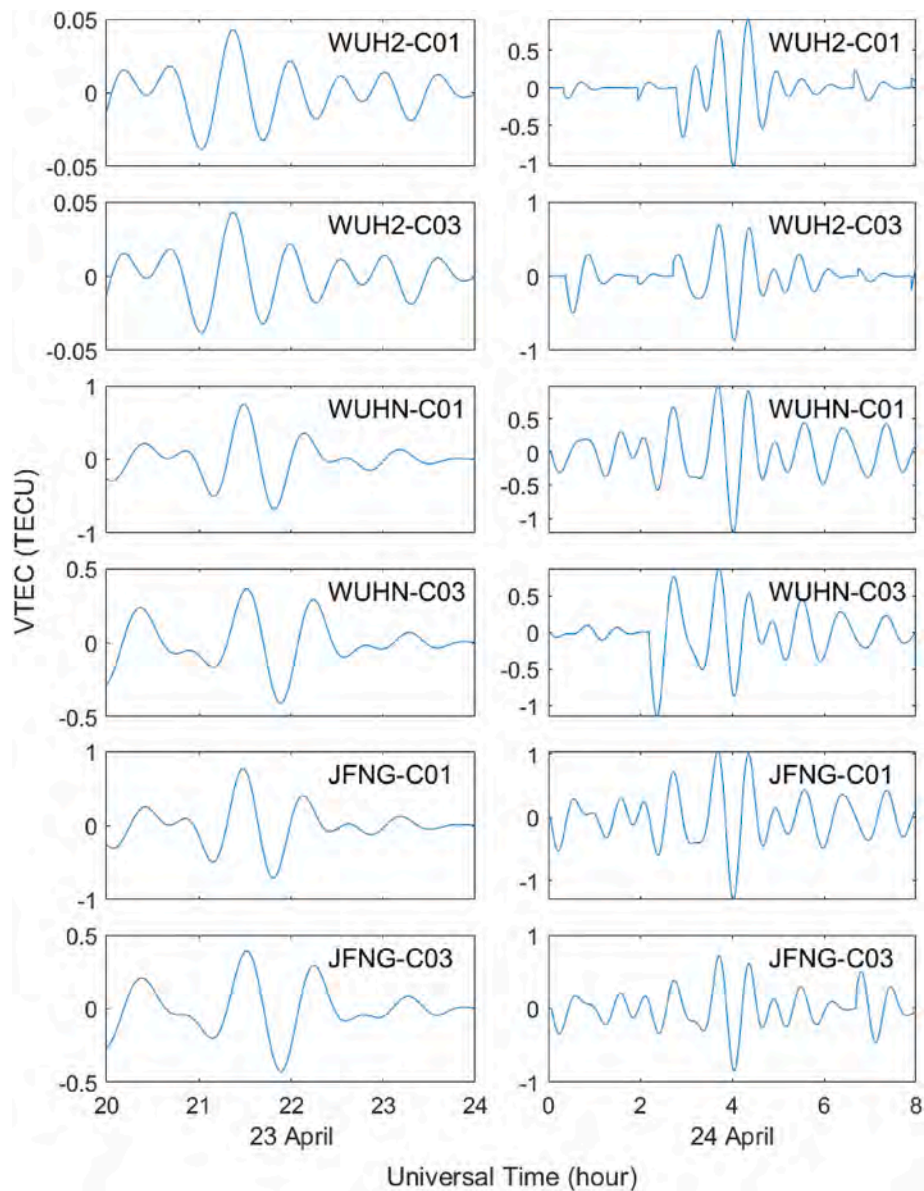
Fig. 6. Obvious TIDs at about 28.4 N from UT = 20–24 on April 23, 2023 (left panel) and UT = 0–8 on April 24, 2023 (right panel), respectively.

decreased around 5 MHz when compared to the quiet day.

Fig. 10 shows the variation in the ionospheric electron density derived from Swarm-A and Swarm-C during April 2023 storm along the Asian longitude sector. The red and black dots represent the quiet and active days, respectively. Compared with the quiet day, which is April 21, 2023, the electron density dropped throughout the main phase.

Fig. 11 illustrates the change of electron density during the storm in the Asian sector. Compared with the quiet day on April 21, 2023, the electron density decreased during the main phase in the F region. Because the COSMIC can also give the electron density data with altitude, it is seen that the height of maximum electron density rises, changing from about 360 km to 450 km. The rise in the height of maximum electron density from COSMIC data revealed an uplift in the ionospheric F layer.

3.4. [O]/[N₂] variations

The column density ratio $[O]/[N_2]$ is essential for comprehending how the ionosphere reacts to geomagnetic disturbances because it reflects the generation and destruction of plasma in the F region of the ionosphere (Rishbeth, 1998). The changes in $[O]/[N_2]$ between April 22, 2023 and April 25, 2023, are shown in Fig. 12. The main change in the Asian sector appeared on April 24, 2023. The $[O]/[N_2]$ ratio showed great change on April 24, 2023, which decreased by about 0.2 in the mid-high latitude region and increased by about 0.2 in the equatorial region. The increase in TEC in the Asian sector during the storm may also have been influenced by the change in neutral composition. As the recombination rate is well connected with neutral components, the generation rate of charged particles in the ionosphere has a positive relationship with oxygen atoms. Therefore, when $[O]/[N_2]$ drops, the electron concentration also drops considerably, indicating a negative storm.

4. Discussion

The results show a negative storm in this study. The F layer lifted and the EIA occurred on April 24, 2023. It is indicated that the fluctuations in electron density is resulted from a number of physical processes. The plasma drifted upward and the ionosphere lifted as a result of the eastward electric field E and the south-north magnetic field B (Tsurutani et al., 2004). Because of the various densities at different heights, the
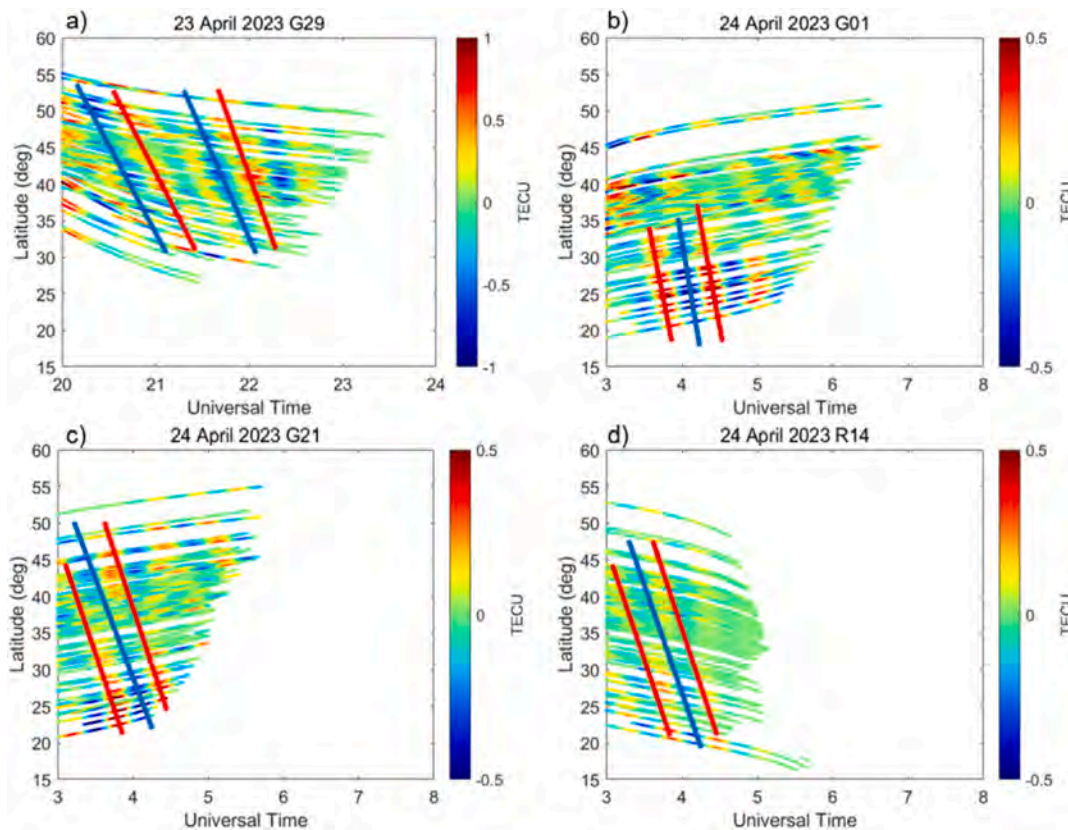
Fig. 7. Travel gram from G29 on April 23, 2023 from UT = 20–24 (a), G01 (b), G21 (c), and R14 (d) on April 24, 2023 from UT = 3–8.
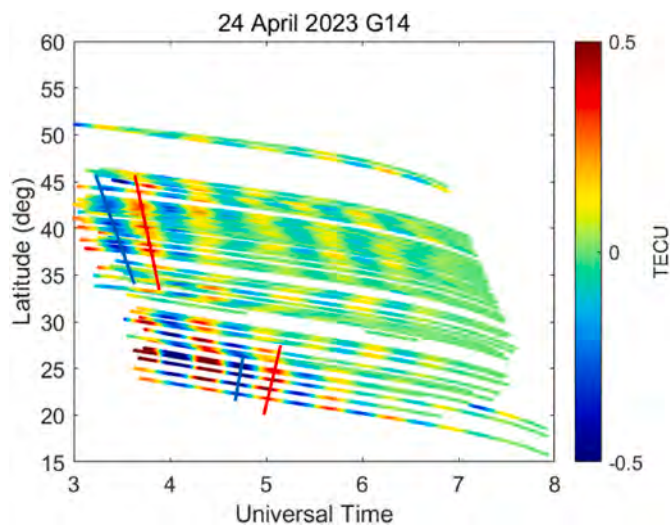

Fig. 8. Travel gram from G14 on April 24, 2023 from UT = 3–8.

plasma flowed to the northern and southern hemispheres and dropped there with the impact of gravity and the pressure gradient force. Therefore, there were more TEC in the middle latitude region than in the equatorward region, which is called fountain effect. Besides, the disturbance dynamo electric field (DDEF) and prompt penetration electric field (PPEF) are the main mechanisms that govern equatorial electrodynamic effects during a storm. Both amplitude and latitude of the EIA are intensified by PPEF (Tulasi Ram et al., 2019). The over shielding electric field enters the low latitude with polarity westward or eastward on the dayside or nightside during northward IMF Bz. The vertical E × B plasma drift is significantly affected by PPEF. The

thermospheric wind is stronger in the mid-latitude region, while the PPEF is more significant in the dayside sub-auroral and low-latitude region, according to Lu et al. (2012), who used the thermosphere-ionosphere-mesosphere-electrodynamics general circulation model (TIEGCM). It is generally believed that changes in the thermosphere's composition, specifically a decline in the $[O]/[N_2]$ ratio, are the cause of negative ionospheric storms. Some early investigations also supported it (Fuller-Rowell et al., 1994; Astafyeva et al., 2015).

In this study, both equatorward propagating LSTIDs and poleward propagating LSTIDs are observed during the April 2023 magnetic storm in Asian sector. According to Hocke and Schlegel (1996), AGWs stimulated from auroral regions in various hemispheres are thought to be the primary source of LSTIDs. Thus, the LSTIDs could propagate from high latitude to low latitude. Haralambous and Paul (2023) showed that the auroral current and precipitating particles were crucial in providing the energy source for these LSTIDs. The increased heating rate in the atmosphere leads to a rise in the auroral temperature, which in turn enhances the activity of AGWs. The AGWs, with large amplitudes, generate TIDs in the ionosphere (Hines, 1960). Compared with the equatorward propagating LSTIDs, the poleward LSTIDs are relatively less studied and the physical mechanism is also intricate. Habarulema et al. (2015, 2016) demonstrated that the equatorial electrojet (EEJ), with possible modulation from the development of the equatorward ionization anomaly area, is the fundamental cause of the poleward propagating large-scale TIDs. However, Jonah et al. (2018) have noted the poleward TIDs that may be linked to local AGWs produced by convective activity as well as the two-direction MSTIDs that occurred over North America in May 2017. Additionally, energy loss during the propagation of TIDs in the polarity direction may be a cause of negative storms discovered by GIM and ionosonde (Habarulema et al., 2015).

Fig. 13 illustrates the solar wind velocity, dawn-to-dusk component of Interplanetary electric field (IEF) and IMF Bz from ACE data. The IEF values increased greatly as a result of the increased solar wind velocities
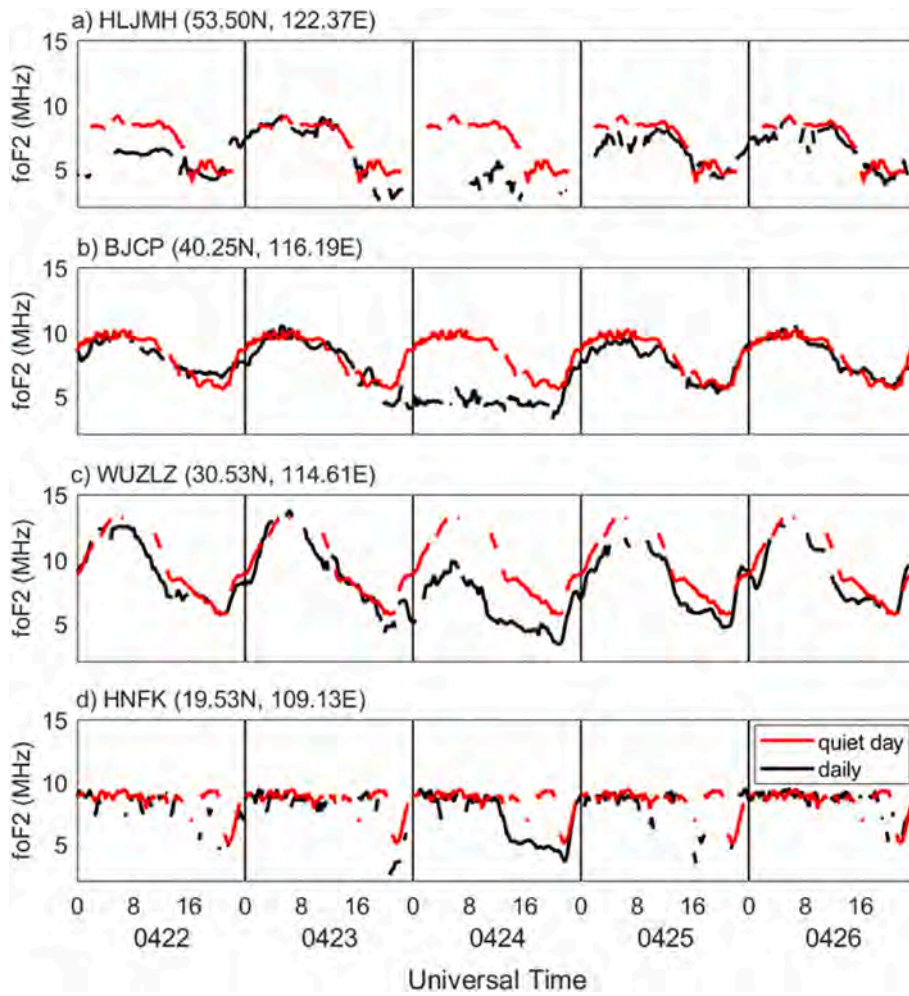
Fig. 9. The foF2 from (a) Heilongjiang Mohe, (b) Beijing Changping, (c) Wuhan Zuolingzhen and, (d) Hainan Fuke during 22–26 April 2023 (black line) and quiet day (April 21, 2023, red line). (For interpretation of the references to colour in this figure legend, the reader is referred to the Web version of this article.)
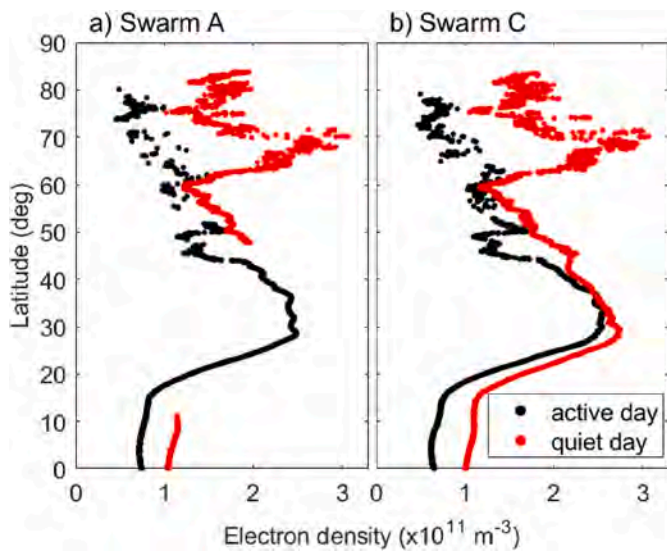

Fig. 10. Electron density from the active day (black dots) and quiet day (red dots) of (a) Swarm A and (b) Swarm C. And there is no Swarm B data during the period. (For interpretation of the references to colour in this figure legend, the reader is referred to the Web version of this article.)
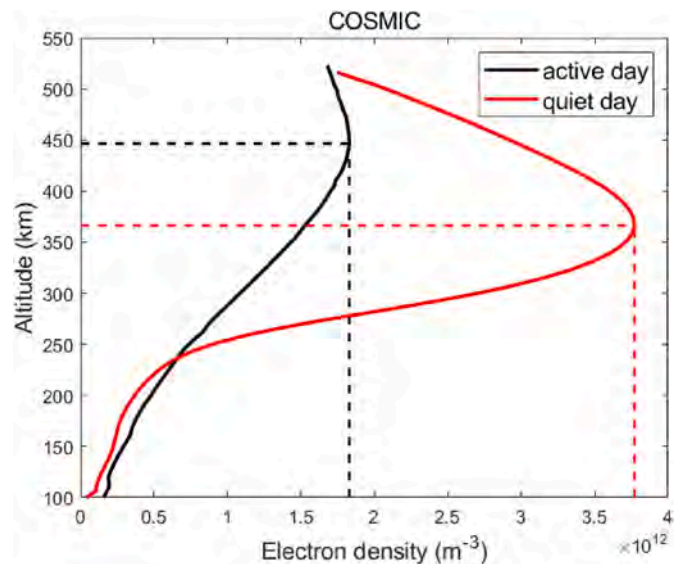
Fig. 11. Electron density from the active day (black line) and quiet day (red line) from COSMIC. (For interpretation of the references to colour in this figure legend, the reader is referred to the Web version of this article.)
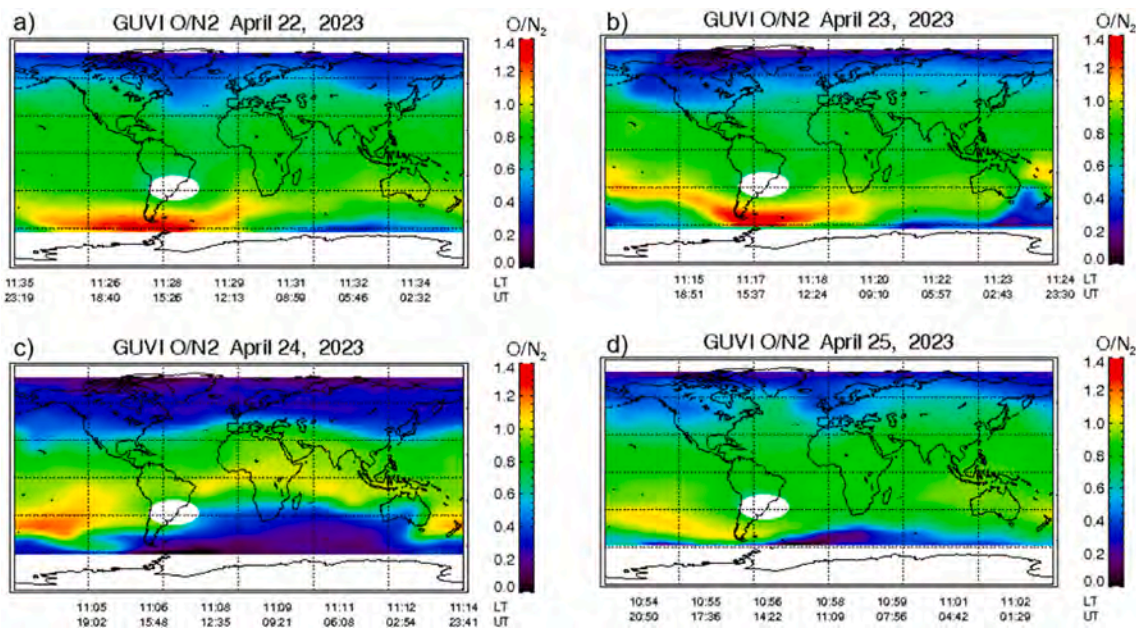
Fig. 12. The $[O]/[N_2]$ ratio obtained from GUVI/TIMED during 22–25 April 2023. The blank region lacks the data. The white oval in (a)–(d) is marked as South Atlantic Anomaly where the GUVI data were contaminated by particle hit noise.
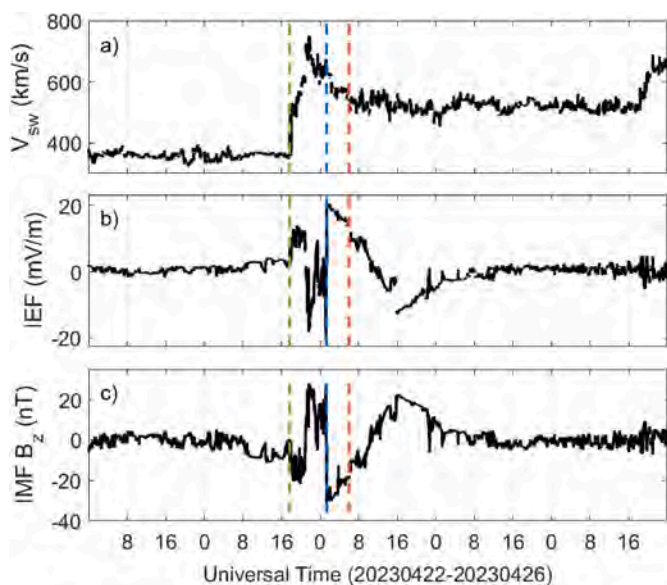

Fig. 13. Solar wind velocity (a), electric field (b), and IMF Bz orientation (c) from ACE data. The red line is the minimum Dst time, and the green line and blue line represent the sharp change moment of Bz and IEF. (For interpretation of the references to colour in this figure legend, the reader is referred to the Web version of this article.)

accompanied by the storm (Tsurutani et al., 2014). Large IEFs could cause penetration electric fields in the magnetosphere and ionosphere with continuing for several hours. The interaction of the solar wind, magnetosphere, and ionosphere is indicated by the high IEF values that might immediately enter the magnetosphere-ionosphere system and travel to middle and low/equatorward latitudes (Habarulema et al., 2016). The IMF Bz gradually went northward from UT = 21:00 on 23 April as Fig. 13 demonstrated. Around UT = 01:15 on 24 April, the IMF Bz turned southward quickly, which could enhance the $\overrightarrow{E} \times \overrightarrow{B}$ drift and launched AGWs, which was reported in early study (Habarulema et al., 2015). Furthermore, it has been suggested that the IEF could keep

reaching low latitudes without shielding as long as IMF Bz moving southward during the storm. More direct evidence and investigation on the emergence of the poleward TIDs are still required in the future.

Here several multi-instruments are utilized to analyze ionospheric responses to the April 2023 magnetic storm, which shows a negative storm with F layer rising. Through paired BDS GEO satellite data, it was discovered that there is no local east-west direction TIDs. In the meantime, not only the equatorward LSTIDs appeared, but also the poleward LSTIDs propagated. Furthermore, to better understand these reactions and comprehensive physical mechanisms of ionospheric behaviors and characteristics in Asian sector during the April 2023 geomagnetic storm, we will further conduct numerical simulation and investigations using TIEGCM and the Global Ionosphere-Thermosphere Model (GITM) in the future (Ridley et al., 2006; Yuan and Jin, 2021).

5. Conclusions

In this study, the ionospheric responses and variation characteristics following the April 2023 geomagnetic storm are studied in details along Asian sector with multi-instruments observation data. The main results and findings are summarized as follows.

1. Significant LSTIDs are observed from BDS GEO satellites, GPS, and GLONASS. On April 24, 2023 at 05:30, the Dst approached the minimum value, and greater amplitude of TIDs is observed from BDS GEO satellites observations.
2. Negative storm is observed in the mid-latitude region and the $[O]/[N_2]$ ratio changes during the main phase. In the mid-high latitude area, the ratio is dropped by around 0.2, whereas in the equatorial region, it is climbed by approximately 0.2. The increase in the electron and ion temperatures and drop in the $[O]/[N_2]$ ratio during the storm with speeding up chemical recombination indicate the negative storm.
3. The F region is lifted during the storm. As COSMIC observation data shows, the height of the ionospheric maximum electron density rises by around 80 km when compared to the calm days, which may be driven by the PPEF.
4. The LSTIDs propagate in two directions. The equatorward LSTIDs are caused by the propagation of AGWs from the auroral region, while

the poleward LSTIDs are probably caused by the electrodynamics during the storm. LSTIDs are moved from high latitude regions to low latitude regions at a speed of 760–1300 m/s. The speed of the poleward TID is around 600–750 m/s with about 40 min.

CRediT authorship contribution statement

Linlin Li: Writing – original draft, Software, Methodology. **Shuanggen Jin:** Writing – review & editing, Funding acquisition.

Declaration of competing interest

The authors declare that they have no known competing financial interests or personal relationships that could have appeared to influence the work reported in this paper.

Data availability

Data used in this paper are public and the source websites are given.

Acknowledgments

References

Alizadeh, M.M., Schuh, H., Todorova, S., Schmidt, M., 2011. Global Ionosphere Maps of VTEC from GNSS, satellite altimetry, and formosat-3/COSMIC data. J. Geodesy 85 (12), 975–987. https://doi.org/10.1007/s00190-011-0449-z.

Astafyeva, E., Yasyukevich, Y., Maksikov, A., Zhivetiev, I., 2014. Geomagnetic storms, super-storms, and their impacts on GPS-based navigation systems. Space Weather 12 (7), 508–525. https://doi.org/10.1002/2014sw001072.

Astafyeva, E., Zakharenkova, I., Förster, M., 2015. Ionospheric response to the 2015 St. Patrick's Day storm: a global multi-instrumental overview. J. Geophys. Res.: Space Phys. 120 (10), 9023–9037. https://doi.org/10.1002/2015ja021629.

Brunini, C., Azpilicueta, F.J., 2009. Accuracy assessment of the GPS-based slant total electron content. J. Geodesy 83 (8), 773–785. https://doi.org/10.1007/s00190-008-0296-8.

Cai, X., Burns, A.G., Wang, W., Qian, L., Solomon, S.C., Eastes, R.W., Laskar, F.I., 2021. Investigation of a neutral "Tongue" observed by GOLD during the geomagnetic storm on may 11, 2019. J. Geophys. Res.: Space Phys. 126 (6) https://doi.org/10.1029/2020ja028817.

Chernogor, L.F., 2011. The Earth-atmosphere-geospace system: main properties and processes. Int. J. Rem. Sens. 32 (11), 3199–3218. https://doi.org/10.1080/01431161.2010.541510.

Chernogor, L.F., Rozumenko, V.T., 2008. Earth–atmosphere–geospace as an Open Nonlinear Dynamical System.

Christensen, A.B., Paxton, L.J., Avery, S., Craven, J., Crowley, G., Zhang, Y., 2003. Initial observations with the global ultraviolet imager (GUVI) in the NASA TIMED satellite mission. J. Geophys. Res.: Space Phys. 108 (A12) https://doi.org/10.1029/2003ja009918.

Crowley, G., Hackert, C.L., Meier, R.R., Strickland, D.J., Paxton, L.J., Pi, X., Wene, G., 2006. Global thermosphere-ionosphere response to onset of 20 November 2003 magnetic storm. J. Geophys. Res.: Space Phys. 111 (A10) https://doi.org/10.1029/2005ja011518.

Ding, F., Wan, W., Ning, B., Wang, M., 2007. Large-scale traveling ionospheric disturbances observed by GPS total electron content during the magnetic storm of 29-30 October 2003. J. Geophys. Res.: Space Phys. 112 (A6) https://doi.org/10.1029/2006ja012013.

Emelyanov, L.Y., Katsko, S.V., Lyashenko, M.V., Chernogor, L.F., 2023. Ionosphere response to geospace storm on 25 September 2016 over Kharkiv (Ukraine). Adv. Space Res. 71 (8), 3323–3345. https://doi.org/10.1016/j.asr.2023.02.004.

Fuller-Rowell, T.J., Codrescu, M.V., Moffett, R.J., Quegan, S., 1994. Response of the thermosphere and ionosphere to geomagnetic storms. J. Geophys. Res.: Space Phys. 99 (A3) https://doi.org/10.1029/93ja02015.

Habarulema, H.B., Katamzi, Z.T., Yizengaw, E., 2015. First observations of poleward large-scale traveling ionospheric disturbances over the African sector during geomagnetic storm conditions. J. Geophys. Res.: Space Phys. 120 (8), 6914–6929. https://doi.org/10.1002/2015JA021066.

Habarulema, J.B., Katamzi, Z.T., Yizengaw, E., Yamazaki, Y., Seemala, G., 2016. Simultaneous storm time equatorward and poleward large-scale TIDs on a global scale. Geophys. Res. Lett. 43 (13), 6678–6686. https://doi.org/10.1002/2016gl069740.

Haralambous, H., Paul, K.S., 2023. Travelling ionospheric disturbance direction of propagation detection using Swarm A-C in-situ electron density. Rem. Sens. 15 (4) https://doi.org/10.3390/rs15040897.

Heki, K., Enomoto, Y., 2015. Mw dependence of the preseismic ionospheric electron enhancements. J. Geophys. Res.: Space Phys. 120 (8), 7006–7020. https://doi.org/10.1002/2015JA021353.

Heise, S., Jakowski, N., Wehrenpfennig, A., Reigber, C., Lühr, H., 2002. Sounding of the topside ionosphere/plasmasphere based on GPS measurements from CHAMP: initial results. Geophys. Res. Lett. 29 (14) https://doi.org/10.1029/2002gl014738, 44-41-44-44.

Hines, C.O., 1960. Internal Atmospheric gravity waves at ionospheric heights. Can. J. Phys. 38.

Hocke, K., Schlegel, K., 1996. A review of atmospheric gravity waves and travelling ionospheric disturbances: 1982-1995. Ann. Geophys. 14 (9), 917–940. https://doi.org/10.1007/s00585-996-0917-6.

Horvath, I., Lovell, B.C., 2009. Investigating the relationships among the South Atlantic Magnetic Anomaly, southern nighttime midlatitude trough, and nighttime Weddell Sea Anomaly during southern summer. J. Geophys. Res.: Space Phys. 114 (A2) https://doi.org/10.1029/2008ja013719.

Hunsucker, R.D., 1982. Atmospheric gravity waves generated in the high-latitude Ionosphere: a review. Rev. Geophys. Space Phys. 20, 293–315.

Jin, S.G., Park, J., Wang, J., Choi, B., Park, P., 2006. Electron density profiles derived from ground-based GPS observations. J. Navig. 59 (3), 395–401. https://doi.org/10.1017/S0373463306003821.

Jin, S.G., Park, J., 2007. GPS ionospheric tomography: a comparison with the IRI-2001 model over South Korea. Earth Planets Space 59 (4), 287–292. https://doi.org/10.1186/BF03353106.

Jin, S.G., Jin, R., Kutoglu, H., 2017. Positive and negative ionospheric responses to the March 2015 geomagnetic storm from BDS observations. J. Geodesy 91 (6), 613–626. https://doi.org/10.1007/s00190-016-0988-4.

Jin, S.G., Wang, Q., Dardanelli, G., 2022. A review on multi-GNSS for Earth observation and emerging applications. Rem. Sens. 14 (16), 3930. https://doi.org/10.3390/rs14163930.

Jonah, O.F., Coster, A., Zhang, S., Goncharenko, L., Erickson, P.J., Paula, E.R., Kherani, E.A., 2018. TID observations and source analysis during the 2017 memorial day weekend geomagnetic storm over North America. J. Geophys. Res.: Space Phys. 123 (10), 8749–8765. https://doi.org/10.1029/2018ja025367.

Liu, L., Zou, S., Yao, Y., Aa, E., 2019. Multi-scale ionosphere responses to the May 2017 magnetic storm over the Asian sector. GPS Solut. 24 (1) https://doi.org/10.1007/s10291-019-0940-1.

Lu, G., Goncharenko, L., Nicolls, M.J., Maute, A., Coster, A., Paxton, L.J., 2012. Ionospheric and thermospheric variations associated with prompt penetration electric fields. J. Geophys. Res.: Space Phys. 117 (A8) https://doi.org/10.1029/2012ja017769.

Ma, R., Xu, J., Wang, W., Lei, J., 2012. The effect of ~27 day solar rotation on ionosphericF2region peak densities (NmF2). J. Geophys. Res.: Space Phys. 117 (A3) https://doi.org/10.1029/2011ja017190.

Nicolls, M.J., Kelley, M.C., Coster, A.J., González, S.A., Makela, J.J., 2004. Imaging the structure of a large-scale TID using ISR and TEC data. Geophys. Res. Lett. 31 (9) https://doi.org/10.1029/2004gl019797.

Ren, X., Mei, D., Liu, H., Zhang, X., 2022. Investigation on horizontal and vertical traveling ionospheric disturbances propagation in global-scale using GNSS and multi-LEO satellites. Space Weather 20 (5). https://doi.org/10.1029/2022sw003041.

Ridley, A.J., Deng, Y., Tóth, G., 2006. The global ionosphere–thermosphere model. J. Atmos. Sol. Terr. Phys. 68 (8), 839–864. https://doi.org/10.1016/j.jastp.2006.01.008.

Rishbeth, H., 1998. How the thermospheric circulation affetcs the ionospheric F2-layer. J. Atmos. Sol. Terr. Phys. 60 (14), 1385–1402. https://doi.org/10.1016/s1364-6826(98)00062-5.

Somsikov, V., 1987. A spherical model of wave generation in the atmosphere by the solar terminator. J. Atmos. Terr. Phys. 49 (5), 433–438. https://doi.org/10.1016/0021-9169(87)90037-7.

Skone, S., Yousuf, R., 2007. Performance of satellite-based navigation for marine users during ionospheric disturbances. Space Weather 5 (1). https://doi.org/10.1029/2006sw000246.

Shinbori, A., Otsuka, Y., Sori, T., et al., 2022. Electromagnetic conjugacy of ionospheric disturbances after the 2022 Hunga Tonga-Hunga Ha'apai volcanic eruption as seen in GNSS-TEC and SuperDARN Hokkaido pair of radars observations. Earth Planets Space 74 (1), 1–17. https://doi.org/10.1186/s40623-022-01665-8.

Su, K., Jin, S.G., Hoque, M., 2019. Evaluation of ionospheric delay effects on multi-GNSS positioning performance. Rem. Sens. 11 (2), 171. https://doi.org/10.3390/rs11020171.

Tang, J., Gao, X., Li, Y., Zhong, Z., 2022. Study of ionospheric responses over China during September 7–8, 2017 using GPS, Beidou (GEO), and Swarm satellite observations. GPS Solut. 26 (2) https://doi.org/10.1007/s10291-022-01244-0.

Tsurutani, B.T., Echer, E., Shibata, K., Verkhoglyadova, O.P., Mannucci, A.J., Gonzalez, W.D., Kozyra, J.U., Patzold, M., 2014. The interplanetary causes of geomagnetic activity during the 7-17 March 2012 interval: a CAWSES II Overies. J. Space Weather Space Clim. 4 (A02), A02p1–A02p7. https://doi.org/10.1051/swsc/2013056.

Tsugawa, T., Saito, A., 2004. A statistical study of large-scale traveling ionospheric disturbances using the GPS network in Japan. J. Geophys. Res.: Space Phys. 109 (A6) https://doi.org/10.1029/2003ja010302.

Tsugawa, T., Saito, A., Otsuka, Y., Yamamoto, M., 2003. Damping of large-scale traveling ionospheric disturbances detected with GPS networks during the geomagnetic storm. J. Geophys. Res.: Space Phys. 108 (A3) https://doi.org/10.1029/2002ja009433.

Tsurutani, B., Mannucci, A., Byron, I., Ali, A.M., Humberto, S.J.A., Walter, G., M V V, 2004. Global dayside ionospheric uplift and enhancement associated with interplanetary electric fields. J. Geophys. Res.: Space Phys. 109 (A8) https://doi.org/10.1029/2003ja010342.

Tulasi Ram, S., Nilam, B., Balan, N., Zhang, Q., Shiokawa, K., Chakrabarty, D., Yoshikawa, A., 2019. Three different episodes of prompt equatorial electric field perturbations under steady southward IMF Bz during St. Patrick's Day storm. J. Geophys. Res.: Space Phys. 124 (12), 10428–10443. https://doi.org/10.1029/2019ja027069.

Valladares, C.E., Hei, M.A., 2012. Measurement of the characteristics of TIDs using small and regional networks of GPS receivers during the campaign of 17–30 July of 2008. Int. J. Geophys. 1–14. https://doi.org/10.1155/2012/548784.

Yuan, L.L., Jin, S.G., 2021. Observational evidence and formation mechanism of low-density cells in the upper thermosphere on 8 September 2017. J. Geophys. Res. Space Phys. 126 (2), e2020JA028915 https://doi.org/10.1029/2020JA028915.